Direct Kinetic Measurements and Master Equation Modelling of the Unimolecular Decomposition of Resonantly-Stabilized CH2CHCHC(O)OCH3 Radical and an Upper Limit Determination for CH2CHCHC(O)OCH3 + O-2 Reaction

Joshi, Satya Prakash

Österreichische Akademie der Wissenschaften

2020-07

Joshi, S P, Seal, P, Pekkanen, T T, Timonen, R S & Eskola, A J 2020, 'Direct Kinetic Measurements and Master Equation Modelling of the Unimolecular Decomposition of Resonantly-Stabilized CH2CHCHC(O)OCH3 Radical and an Upper Limit Determination for CH2CHCHC(O)OCH3 + O-2 Reaction', Zeitschrift für physikalische Chemie, vol. 234, no. 7-9, pp. 1251-1268. https://doi.org/10.1515/zpch-2020-1612

http://hdl.handle.net/10138/329666
10.1515/zpch-2020-1612

acceptedVersion

Satya Prakash Joshi, Prasenjit Seal, Timo Theodor Pekkanen, Raimo Sakari Timonen and Arkke Johannes Eskola*

Direct Kinetic Measurements and Master Equation Modelling of the Unimolecular Decomposition of Resonantly-Stabilized $CH_2CHCHC(O)OCH_3$ Radical and an Upper Limit Determination for $CH_2CHCHC(O)OCH_3 + O_2$ Reaction

https://doi.org/10.1515/zpch-2020-1612
Received January 15, 2020; accepted March 16, 2020

Abstract: Methyl-Crotonate (MC, (*E*)-methylbut-2-enoate, $CH_3CHCHC(O)OCH_3$) is a potential component of surrogate fuels that aim to emulate the combustion of fatty acid methyl ester (FAME) biodiesels with significant unsaturated FAME content. MC has three allylic hydrogens that can be readily abstracted under autoignition and combustion conditions to form a resonantly-stabilized $CH_2CHCHC(O)OCH_3$ radical. In this study we have utilized photoionization mass spectrometry to investigate the O_2 addition kinetics and thermal unimolecular decomposition of $CH_2CHCHC(O)OCH_3$ radical. First we determined an upper limit for the bimolecular rate coefficient of $CH_2CHCHC(O)OCH_3 + O_2$ reaction at 600 K ($k \leq 7.5 \times 10^{-17}$ cm^3 molecule^{-1} s^{-1}). Such a small rate coefficient suggest this reaction is unlikely to be important under combustion conditions and subsequent efforts were directed towards measuring thermal unimolecular decomposition kinetics of $CH_2CHCHC(O)OCH_3$ radical. These measurements were performed between 750 and 869 K temperatures at low pressures (<9 Torr) using both helium and nitrogen bath gases. The potential energy surface of the unimolecular decomposition reaction was probed at density functional (MN15/cc-pVTZ) level of theory and the electronic energies of the stationary points obtained were then refined using the DLPNO-CCSD(T) method with the cc-pVTZ and cc-pVQZ basis sets. Master equation simulations were subsequently carried out using MESMER code along the kinetically important reaction pathway. The master equation model was first optimized by fitting the zero-point energy corrected reaction barriers

***Corresponding author: Arkke Johannes Eskola,** Department of Chemistry, University of Helsinki, P.O. Box 55 (A.I. Virtasen aukio 1), FI-00014, Helsinki, Finland, e-mail: arkke.eskola@helsinki.fi. https://orcid.org/0000-0002-2249-2726
Satya Prakash Joshi, Prasenjit Seal, Timo Theodor Pekkanen and Raimo Sakari Timonen: Department of Chemistry, University of Helsinki, P.O. Box 55 (A.I. Virtasen aukio 1), FI-00014, Helsinki, Finland

and the collisional energy transfer parameters $\Delta E_{\text{down, ref}}$ and n to the measured rate coefficients data and then utilize the constrained model to extrapolate the decomposition kinetics to higher pressures and temperatures. Both the experimental results and the MESMER simulations show that the current experiments for the thermal unimolecular decomposition of $CH_2CHCHC(O)OCH_3$ radical are in the fall-off region. The experiments did not provide definite evidence about the primary decomposition products.

Keywords: $CH_2CHCHC(O)OCH_3$ radical; fatty acid methyl ester; master equation modelling; photo-ionization-mass-spectrometer; unimolecular decomposition.

1 Introduction

Bio-fuels derived from non-edible plant oils are promising alternative fuels to supplement or replace conventional fossil fuels due to their renewable nature and lower particulate matter (PM) emission characteristics [1, 2]. Contemporary commercial bio-fuels contain saturated and unsaturated fatty acid methyl esters (FAMEs) as major components and can be mixed with conventional fossil fuels. FAMEs are produced by esterifying fatty acids present in vegetable oils [3]. This process is essential for increasing the overall performance of bio-fuels as FAMEs are less corrosive to the combustion engines and have significantly lower ignition delay times than simple fatty acids [4]. Standard commercial bio-fuels usually contain saturated and unsaturated, relatively complicated long-chain FAMEs (C_{14}–C_{22}). This complexity makes it difficult to understand their combustion properties in detail [5]. To address this problem, surrogate fuel models have been constructed to emulate the autoignition and combustion chemistry of complicated bio-fuels [6, 7]. Methyl-Crotonate (MC, (*E*)-methylbut-2-enoate, $CH_3CHCHC(O)OCH_3$), an unsaturated C_4-ester, is a potential component of such a surrogate fuel model.

The flame chemistry and the high-temperature combustion of MC have been studied using shock-tubes, different flame techniques, and jet-stirred reactors (JSR) [8–14]. Little is known about the low-temperature combustion (LTC) of MC, although JSR experiments indicate that MC experiences some LTC chemistry [8]. Under combustion conditions MC undergoes hydrogen-atom abstraction *via* reaction with atoms and radicals such as: H, O, OH, R, RO_2, etc. As shown in Scheme 1, MC has three allylic hydrogens, two distinct vinylic hydrogens, and three alkylic hydrogens available for abstraction.

The allylic and the alkylic hydrogens have the lowest and second lowest bond enthalpies, respectively (87.7 and 100 kcal/mol) [12]. A recent theoretical study by

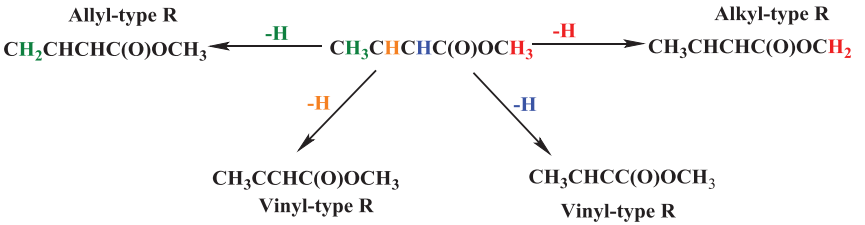

Scheme 1: H-atom abstraction reactions from MC produce four different types of radicals.

Zhou et al. [15] on the kinetics of OH + MC reaction shows that the abstraction of one of the allylic hydrogens is the dominant reaction pathway over a wide range of conditions (500–1800 K and 0.001–100 atm).

As Scheme 2 shows, the highly resonantly-stabilized structure of the $CH_2CHCHC(O)OCH_3$ radical suggest that under LTC conditions its bimolecular reaction with molecular oxygen (O_2) may be very slow. For instance, Knyazev et al. [16] measured an upper limit of 2×10^{-16} cm^3 molecule^{-1} s^{-1} for the bimolecular rate coefficient of 1-methylallyl + O_2 reaction at 700 K. Hence, while modeling autoignition chemistry and combustion of such radicals, the contribution of thermal unimolecular decomposition reaction may play an important role.

$$CH_2CHCHC(O)OCH_3 + M(He,\ N_2) \xrightarrow{k_{unim.}} \text{Products} \qquad (1)$$

In this study, we have measured a low upper limit for the bimolecular rate coefficient of the $CH_2CHCHC(O)OCH_3 + O_2$ reaction (2) at 600 K. The LTC chemistry of the $CH_2CHCHC(O)OCH_3$ was further studied by performing the first direct kinetic measurements of the thermal unimolecular decomposition of $CH_2CHCHC(O)OCH_3$ radical as a function of temperature and bath gas density. Both helium and nitrogen bath gases were used in the measurements. The experimental results of the thermal unimolecular decomposition kinetics were complemented with quantum-chemistry calculations and master equation modelling.

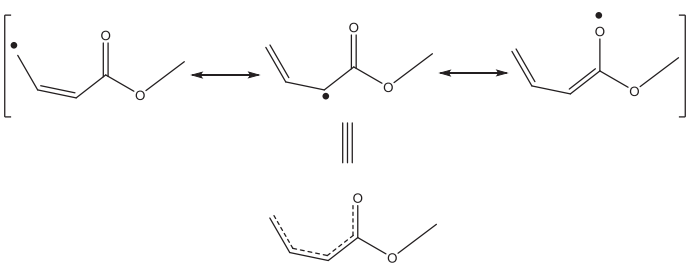

Scheme 2: Resonance structures of the $CH_2CHCHC(O)OCH_3$ radical.

2 Experimental

The experimental apparatus employed in the current measurements is a photoionization-mass-spectrometer (PIMS) coupled with a laminar flow reactor. The PIMS setup has been described previously [17], so only details relevant to the current study will be discussed here.

In the kinetic measurements of reaction (1), the reaction mixture flowing through the laminar flow rector consisted mainly (>99.7%) of the bath gas (Helium or N_2) and only a small amount of precursor (<0.3%) was present. In the upper limit experiment a similar amount of precursor was used, but a significant portion of the reaction mixture consisted of O_2 (<37%). The resonantly-stabilized $CH_2CHCHC(O)OCH_3$ radical was produced along the reactor axis by 248 nm excimer laser (COMPex 201) photolysis of methyl 5-methylhex-2-enoate, $(CH_3)_2CHCH_2CHCHC(O)OCH_3$ ($m/z = 142$). In addition to the $CH_2CHCHC(O)OCH_3$ radical observed at $m/z = 99$, photolysis products were observed at $m/z = 43$ and $m/z = 141$, which are expected to originate from $(CH_3)_2CH$ and $(CH_3)_2CHCHCHCHC(O)OCH_3$ radicals, respectively.

$$(CH_3)_2CHCH_2CHCHC(O)OCH_3 + h\nu_{248\ nm}$$
$$\rightarrow CH_2CHCHC(O)OCH_3 + (CH_3)_2CH \quad \text{(P1a)}$$
$$\rightarrow \text{Other products} \quad \text{(P1b)}$$

In addition to the thermal unimolecular decomposition and O_2 addition reactions, the self-reaction of the radical (A) and heterogeneous wall reactions (B) contribute to the loss of $CH_2CHCHC(O)OCH_3$.

$$R + R \rightarrow \text{Products} \quad \text{(A)}$$

$$R \rightarrow \text{Heterogeneous loss} \quad \text{(B)}$$

In order to minimize reaction (A), low precursor concentrations were used to keep radical concentrations low. This ensured that the observed decay of $CH_2CHCHC(O)OCH_3$ radical was single-exponential and depended only on the employed temperature and bath gas density.

The thermal unimolecular decomposition rate coefficient measurements were performed between 750 and 869 K temperatures. Bath gas density ranges of 0.6–10 $\times$ 10^{16} molecules cm^{-3} and 2.6–5 $\times$ 10^{16} molecules cm^{-3} were used for helium and nitrogen, respectively. Boric oxide coated quartz tubes with inner diameters of 0.85 or 1.7 cm were utilized. The reactors were heated using PID controlled resistive heating. In the temperature ranges 750–836 K and 836–869 K the

temperature uniformity of the reaction zone was measured to be ±2 K and ±5 K, respectively.

The $CH_2CHCHC(O)OCH_3$ radical was ionized using a Cl_2-lamp (microwave discharge of Cl_2-helium mixture with a CaF_2 window to produce radiation in the range 8.9–9.1 eV), while potential products were sought using either a H_2-lamp (discharge of H_2 with a MgF_2 window to produce radiation at around 10.2 eV) or an Ar-lamp (discharge of Ar with a LiF window to produce radiation in the range 11.6–11.8 eV). A quadrupole mass-spectrometer was utilized to mass-select ions based on their *m/z* ratio. An electron multiplier was used for temporal ion counting, and an amplifier/discriminator for production of NIM-pulses, which were detected using a multichannel scaler and analyzed in PC. A temporal radical ion decay signal measurement was typically repeated 4000–8000 times and a product formation measurement ~15,000 times to obtain reasonable signal-to-noise ratio with a repetition rate of 5 Hz. Data was collected from 10 ms before to 40 ms after each excimer laser pulse. An exponential function $[R_t] = A + [R_0] \times \exp(-k'_{1,2}t)$ was fitted to the radical ion decay signal by employing nonlinear least-squares method to obtain $k'_{1,2} = k'_1$ or k'_2. For reaction (1), $k'_1 = k_1 + k_{wall}$, where k_1 is the unimolecular reaction rate coefficient at a certain T and P and k_{wall} is the rate coefficient for the heterogeneous wall-loss reactions. For reaction (2), $k'_2 = k_2 \times [O_2] + k_{wall}$, where k_2 is the bimolecular reaction rate coefficient at a certain T and P. A is the signal background. $[R_0]$ and $[R_t]$ are proportional to the initial ($t = 0$) and temporal radical concentration, respectively.

Thermal unimolecular decay of the $CH_2CHCHC(O)OCH_3$ radical starts to become observable at temperatures above 610 K. To calculate the value of k_1 at any particular temperature requires knowledge of k_{wall}. However, the value of k_{wall} cannot be deduced directly under conditions where unimolecular decomposition rate coefficient is significant, i.e. $T > 610$ K. Hence, we assume that k_{wall} remains temperature independent under the temperature range of 610–869 K. In order to minimize any possible errors this assumption introduces, we follow the scheme proposed by Knyazev et al. [18] for locating the lower limit of k'_1 (i.e. $k'_1 \geq 3\ k_{wall}$), at which k_1 can be measured reliably. In our case this lower limit of k'_1 value corresponds to 750 K temperature. Since, with our current experimental set-up the $k'_{1,2}$ values >500 s^{-1} possess larger than desired uncertainty, the upper temperature limit for the thermal unimolecular decay rate measurements was limited to 869 K. An upper limit for the bimolecular rate coefficient of the reaction between $CH_2CHCHC(O)OCH_3$ radical and O_2 was measured at 600 K, just below the temperature where the thermal unimolecular decay of $CH_2CHCHC(O)OCH_3$ becomes relevant.

Before use, the photolytic precursor (methyl 5-methylhex-2-enoate, Apollo Scientific, purity >97%) was degassed with several freeze-pump-thaw cycles. He

(Aga, purity of 99.9996%), N_2 (Aga, purity of 99.999%), and O_2 (Aga, purity of 99.998%) were used as supplied.

3 Computational techniques and master equation simulations

Geometry optimizations and normal mode analysis for the stationary points on the potential energy surface (PES) of reaction (1) were performed using the MN15 density functional with the cc-pVTZ basis set. Subsequently, the obtained vibrational frequencies and zero point energies (ZPE) were scaled with respect to a semi-empirical scaling factor of 0.993 and 0.979, respectively [19]. The electronic energies of the optimized stationary points were further refined with the domain-based local pair natural orbital coupled cluster, DLPNO-CCSD(T) method. Electronic energies were extrapolated to the complete basis set ($E_{\text{total}}^{\text{CBS}}$) using the following equation:

$$E_{\text{total}}^{\text{CBS}}(X,\ X+1) \approx E_{\text{SCF}}^{\text{CBS}}(X,\ X+1) + E_{\text{corr}}^{(\text{MDCI; CBS})}(X,\ X+1) + (E_{\text{corr}}^{(\text{CCSD(T); } X)} - E_{\text{corr}}^{(\text{MDCI; } X)}) \quad \text{(E1)}$$

Here, X and X + 1 are the basis set cardinal numbers used for the extrapolation. In our case, we used the cc-pVTZ and cc-pVQZ basis sets, hence, X = 3 in the above equation [20]. In order to obtain the self-consistent field (SCF) CBS energy, an extrapolation of the form $E_{\text{SCF}}^{(X)} = E_{\text{SCF}}^{(\infty)} + Ae^{-\alpha\sqrt{X}}$ was used and an optimization of α was done for each pair of basis sets used for extrapolation. For the correlation energy extrapolation, Schwenke's linear combination approach using the equation of the form, $E_{\text{corr}}^{\infty} = \frac{X^{\beta}E_{\text{corr}}^{(X+1)} - (X+1)^{\beta}E_{\text{corr}}^{(X+1)}}{X^{\beta} - (X+1)^{\beta}}$ was implemented and β has been optimized for the same pair of basis sets that was used for the optimization of α.

The DLPNO calculations were performed with ORCA 4.1.1 [21] software and the MN15 calculations were performed using the Gaussian 16 software package [22]. KinBot, an automated reaction pathway generator, was used for searching possible reaction pathways for reaction (1) prior to the optimizations [23].

Master equation simulations (rate calculations) of reaction (1) were performed using MESMER 5.2 code and the PES calculated above was used to obtain a best fit with the experimental rate data by adjusting a few parameters discussed below [24]. MESMER uses Rice–Ramsperger–Kassel–Marcus theory to calculate microcanonical rate coefficients. A harmonic oscillator – rigid rotor approximation was used for all modes except those that correspond to internal rotations. For internal

rotations, 1-D hindered rotor potentials were obtained at the MN15/cc-pVTZ level of theory. MESMER uses a single-exponential down model (E2) to obtain collisional energy transfer probabilities. Energy transfer occurs *via* collisions between a modeled species and bath gas atoms / molecules. Collision frequencies are obtained from a Lennard–Jones (L–J) model.

$$\Delta E_{\text{down}} = \Delta E_{\text{down, ref}} \left(\frac{T}{T_{\text{ref}}} \right)^{n} \tag{E2}$$

In equation (2), ΔE_{down} is the average downward energy transferred per collision, $\Delta E_{\text{down, ref}}$ is the value of ΔE_{down} at T_{ref} (= 298 K) and n is an independent parameter that describes the temperature dependence of ΔE_{down}. If experimental data is provided, MESMER can vary the collisional energy transfer parameters together with transition state energies to obtain values that best reproduce experimental results. A Levenberg–Marquardt fitting algorithm was used to minimize the value of $\chi^2(k_1(\text{exp.}) - k_1(\text{calc.}))^2$.

4 Results and discussion

An upper limit for the bimolecular rate coefficient of $CH_2CHCHC(O)OCH_3 + O_2$ reaction was measured at 600 K. The results are shown in Figure 1 from which an upper limit k_2 (600 K) $\leq 7.5 \times 10^{-17}$ cm^3 molecule^{-1} s^{-1} within 2σ-uncertainty at $p = 5$ Torr pressure is deduced. A low upper limit suggests that other reactions are probably responsible for the loss of $CH_2CHCHC(O)OCH_3$ radical under autoignition and combustion conditions and thermal unimolecular decomposition of $CH_2CHCHC(O)OCH_3$ is potentially such a reaction.

As discussed in the experimental section, for calculating the unimolecular decomposition rate coefficients (k_1) using equation $k'_1 = k_1 + k_{\text{wall}}$, we assume that k_{wall} remains temperature independent under the temperature range of 500–869 K. In order to check the validity of this assumption the measured values of k'_1 are plotted as function of temperature (T = 500–869 K).

As shown in Figure 2, in the temperature range 500–610 K the measured value of k'_1 is uniform (6.1–7.6 s^{-1}). However, above 610 K, a sharp rise in k'_1 is observed, where an exponential increase in k'_1 originates from the strongly temperature-dependent reaction (1) and k'_1 quickly becomes much larger than k_{wall}. This observation shows that any minor change in the value of k_{wall} above 610 K has negligible effect on the obtained values of k_1.

The measured thermal unimolecular decay rate coefficients of reaction (1) are presented in Table 1. The total uncertainties of the k_1 values shown in Table 1 are estimated to be ±25%. This originates mainly from uncertainties in

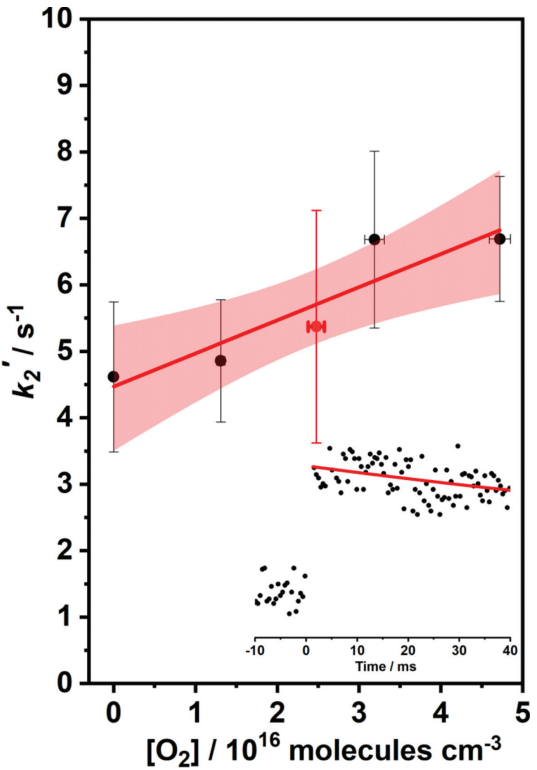

Fig. 1: A bimolecular plot for the $CH_2CHCHC(O)OCH_3 + O_2$ reaction. The measurements were performed at $T = 600$ K and $p = 5$ Torr. The uncertainties shown are 1σ. Here, k'_2 is the pseudo-first-order rate coefficient of reaction (2). A linear fit performed on the data points returns a value of k_2 (600 K) $= (5.1 \pm 1.2\ (1\sigma)) \times 10^{-17}$ cm^3 molecule^{-1} s^{-1} for the slope. Confidence bands shown are within 95%. The inset shows a typical $CH_2CHCHC(O)OCH_3$ radical decay profile together with a single-exponential fit to the data. The decay profile is for the red circle shown in the main figure.

measured temperatures and pressures in the reaction zone as well as from fitting errors.

To rule out a presence of vinyl- or alkyl-type isomers (see Scheme 1), a parallel set of experiments were conducted by adding a high concentration of molecular oxygen, $[O_2] = (1.3 \pm 0.1) \times 10^{15}$ molecules cm^{-3}, to the reaction mixture (labeled as superscript "[d]" in Table 1). An $[O_2]$ this high should rapidly, well within 1 ms, consume all vinyl- and alkyl-type radicals [25]. No difference in unimolecular decay rate coefficients was detected when molecular oxygen was added into the reaction mixture, so we conclude that vinyl- and alkyl-type radicals were not present in the reactor, see Figure S4.

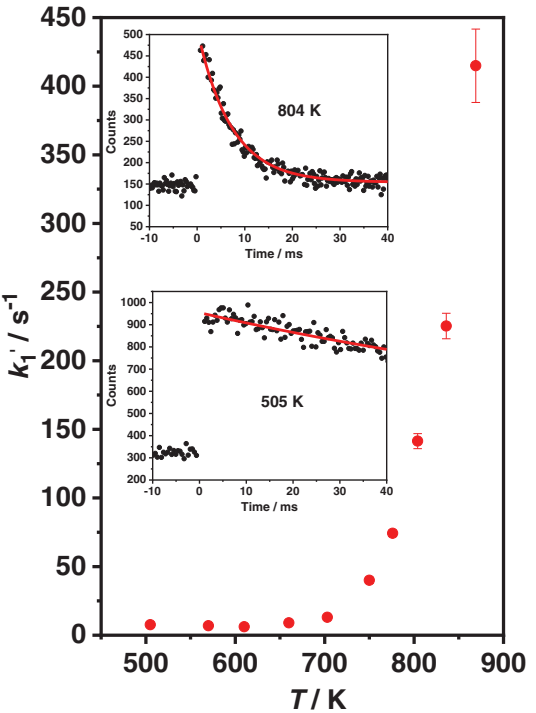

Fig. 2: A plot of the measured values of k'_1 vs. temperature at constant total density. In the insets are presented typical $CH_2CHCHC(O)OCH_3$ radical decay profiles measured at $m/z = 99$ with the corresponding single-exponential decay fits at 505 K (only k_{wall}) and 804 K ($k_1 + k_{wall}$) temperatures, respectively.

A series of experiments were conducted to identify the nature of products formed by reaction (1). However, based upon the experimental results discussed next no definite conclusion about the nature of products was obtained.

Figure 3 presents a potential energy profile for the unimolecular decomposition of $CH_2CHCHC(O)OCH_3$ radical. Here, R_c and R_o are different conformers for $CH_2CHCHC(O)OCH_3$ radical associated with channel (1) and channels (2 & 3), respectively. The calculations show that the most favorable channel produces 2-furanone (P_1, a cyclic $C_4O_2H_4$ compound with $m/z = 84$), a closed shell specie, and a methyl radical (CH_3, $m/z = 15$). However, no direct product signals were observed at parent masses that correspond to these products.

A signal was observed at $m/z = 141$, which sharp increase in intensity immediately after the excimer laser pulse at $t = 0$ ms indicates that all or large majority of the observed signal originates from removal of an allylic H-atom from the precursor molecule with $m/z = 142$ in the photolysis process,

Tab. 1: The results and conditions of the kinetics measurements of reaction (1).[a]

T(K)	[Bath gas]/10^{16} (cm^{-3})	[Pr]/10^{13} (cm^{-3})	k_1 (s^{-1})	k_{wall} (s^{-1})	LI (mJ/cm^2pulse)
He as bath gas					
750[b]	0.65	0.39	12.1 ± 3.2	5.6 ± 1.0	70
750[b]	1.30	0.61	23.2 ± 4.1	5.6 ± 1.0	70
750	2.58	0.97	29.7 ± 0.4	6.7 ± 0.6	70
750	5.15	1.18	33.3 ± 1.7	6.7 ± 0.6	70
750[c]	5.13	0.86	31.2 ± 2.1	7.4 ± 0.6	120
750[c,d]	5.14	0.86	30.9 ± 1.7	7.4 ± 0.6	120
750[c,d]	5.12	1.78	31.3 ± 1.3	16.5 ± 0.7	120
750[c]	5.12	1.79	31.9 ± 1.3	16.5 ± 0.7	120
750	10.3	1.05	37.4 ± 1.6	6.7 ± 0.6	70
776[b]	0.65	0.37	29.6 ± 2.0	7.5 ± 0.8	70
776[b]	1.30	0.53	46.3 ± 3.0	7.5 ± 0.8	70
776	2.62	1.46	57.8 ± 2.3	8.9 ± 0.5	70
776	5.10	1.40	65.4 ± 1.9	8.9 ± 0.5	70
776	10.1	1.19	74.4 ± 2.4	8.9 ± 0.5	70
804[b]	0.64	0.42	60.9 ± 3.5	7.5 ± 0.8	70
804[b]	1.30	0.61	80.7 ± 2.0	7.5 ± 0.8	70
804	2.60	1.31	111 ± 5.7	8.9 ± 0.5	70
804	5.20	1.23	135 ± 4.2	8.9 ± 0.5	70
804[c]	5.16	0.83	134 ± 4.9	7.4 ± 0.6	120
804[c,d]	5.16	0.84	134 ± 4.7	7.4 ± 0.6	120
804[c,d]	5.16	1.91	133 ± 2.9	16.5 ± 0.7	120
804[c]	5.16	1.92	133 ± 3.2	16.5 ± 0.7	120
804	10.3	1.25	157 ± 6.2	8.9 ± 0.5	70
836[b]	1.30	0.66	161 ± 10	7.2 ± 1.3	70
836	2.59	1.01	182 ± 11	5.3 ± 0.7	70
836	5.21	0.91	220 ± 8.6	5.3 ± 0.7	70
836	10.3	1.09	274 ± 13	5.3 ± 0.7	70
860[c]	5.13	0.72	347 ± 23	8.5 ± 0.9	120
860[c, d]	5.13	0.72	350 ± 19	8.5 ± 0.9	120
860[c, d]	5.12	1.80	353 ± 14	16.5 ± 0.7	120
860[c]	5.13	1.80	351 ± 12	16.5 ± 0.7	120
869[b]	1.30	0.75	241 ± 24	5.6 ± 1.0	70
869	2.55	0.89	315 ± 26	6.9 ± 0.7	70
869	5.19	0.86	408 ± 21	6.9 ± 0.7	70
869	10.3	0.66	509 ± 28	6.9 ± 0.7	70
N_2 as bath gas					
750	2.63	1.08	32.2 ± 2.1	15.0 ± 0.8	190
750	5.16	1.18	38.6 ± 2.6	15.0 ± 0.8	190
776	2.62	1.39	57.5 ± 2.8	8.5 ± 0.8	70
776	5.17	1.41	68.5 ± 4.3	8.5 ± 0.8	70
804	2.63	1.45	114 ± 5.8	8.5 ± 0.8	70

Tab. 1 (continued)

T(K)	[Bath gas]/10^{16} (cm^{-3})	[Pr]/10^{13} (cm^{-3})	k_1 (s^{-1})	k_{wall} (s^{-1})	LI (mJ/cm^2pulse)
804	5.16	1.38	138 ± 7.4	8.5 ± 0.8	70
836	2.64	1.44	179 ± 11	8.1 ± 0.8	70
836	5.15	1.31	222 ± 13	8.1 ± 0.8	70
869	2.64	1.32	314 ± 19	8.1 ± 0.8	70
869	5.19	1.29	408 ± 25	8.1 ± 0.8	70

Uncertainties shown are 1σ. [a]Chlorine lamp with a CaF_2 window used for detection, KrF laser (248 nm) for radical production, Quartz reactor with boric acid coating and inner diameter (id) = 0.85 cm used, unless otherwise stated. [b]Quartz reactor with boric acid coating and inner diameter (id) = 1.7 cm. [c]Measurements conducted by varying precursor concentration for ruling out the possibility of reaction between $CH_2CHCHC(O)OCH_3$ radical and precursor molecule. [d]Measurements performed by adding a known amount of molecular oxygen ($[O_2] = (1.3 \pm 0.1) \times 10^{15}$ molecules cm^{-3}) to the reaction mixture.

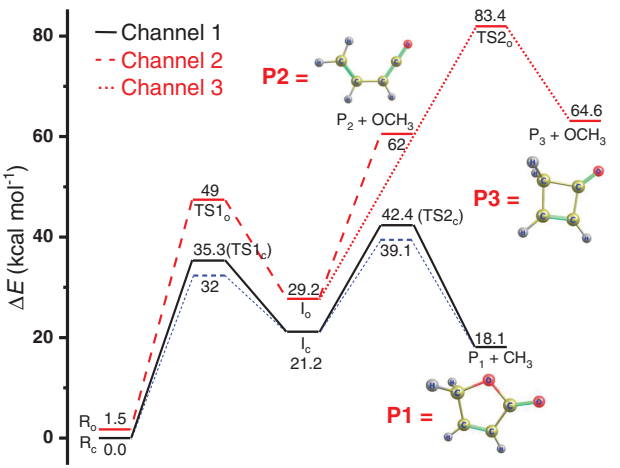

Fig. 3: A zero-point energy inclusive PES for the thermal unimolecular decomposition of $CH_2CHCHC(O)OCH_3$ radical in kcal mol^{-1}. KinBot was used to search for possible reaction channels. The lowest energy reaction pathway found (channel 1) was simulated with MESMER. In order to obtain agreement with the experimental results, the barrier heights of $TS1_c$ and $TS2_c$ were lowered (shown in blue) to 32.0 and 39.1 kcal/mol, respectively, while maintaining the energy gap between the transition states. The red channels (channels 2 and 3) are high-energy reaction channels, which were not included in the master equation model. The optimized geometries and single-point energies of the stationary points are given in the Supplementary Information (see Figure S1 and Table S1).

see Figure S2. Most likely the signal observed at $m/z = 141$ originates from $(CH_3)_2CHCHCHCHC(O)OCH_3$ radical, where a weakly-bonded allylic H-atom is removed in the photolysis. Product measurements were also conducted by adding $[O_2] = (1.4 \pm 0.1) \times 10^{16}$ molecules cm^{-3} to the reaction mixture at 776 K. The bimolecular rate coefficient of $CH_3 + O_2 \longrightarrow CH_3OO$ reaction under these conditions is about $\sim 1 \times 10^{-15}$ cm^3 $molecule^{-1}$ s^{-1} [26], giving about 14 s^{-1} for rate of CH_3OO radical formation. A very weak product formation signal was observed at $m/z = 47$, which could originate from CH_3OO, see Figure S3. However, it is not possible to definitely assign the origin of signal at $m/z = 47$ and consequently methyl radical production to the P1 + CH_3 channel, since the above discussed $(CH_3)_2CHCHCHCHC(O)OCH_3$ radical ($m/z = 141$) may also decompose to $CH_3CHCHCHCHC(O)OCH_3 + CH_3$ products.

It is important to consider if the $CH_2CHCHC(O)OCH_3$ radical could abstract a hydrogen from the precursor, because such a reaction would be an additional loss channel for the radical and affect our thermal unimolecular decomposition rate coefficient measurements. Wang et al. have calculated the kinetics of methyl radical and allyl radical H-atom abstraction reactions from different alkenes [27]. They have found, for example, that $k(CH_3 + CH_3CHCHCH_2CH_3)_{1000\ K} = 2 \times 10^{-14}$ cm^3 $molecule^{-1}$ s^{-1} and $k(CH_2CHCH_2 + CH_3CHCHCH_2CH_3)_{1000\ K} = 5 \times 10^{-16}$ cm^3 $molecule^{-1}$ s^{-1}, where $CH_3CHCHCH_2CH_3$ resembles structure of the current photolytic precursor. Multiplying the above-mentioned bimolecular rate coefficients with the highest precursor concentration utilized in this work, 1.92×10^{13} molecules cm^{-3}, give the rates 0.4 s^{-1} and 0.01 s^{-1}, respectively. These values are far too low to have any effect on the current decomposition kinetic measurements even if these rates are an order of magnitude incorrect for the current system. A set of experiments were conducted (labeled as superscript "[c]" in Table 1) by varying the amount of precursor in the reaction mixture from (0.7–0.9) $\times 10^{13}$ molecules cm^{-3} to (1.8–1.9) $\times 10^{13}$ molecules cm^{-3} in the temperature range 750–860 K at helium density 5.1×10^{16} molecules cm^{-3}. The results of these experiments clearly show that the observed thermal unimolecular decomposition rate coefficient is independent of precursor concentration employed (see Figure S4), which is further evidence that the radical does react with the precursor to any measurable degree.

No product signal was observed at $m/z = 84$ (P1, 2-furanone), although our calculations suggest that the lowest energy channel of reaction (1) should produce 2-furanone (P1). To test if our PIMS apparatus is able to detect this closed-shell molecule, a measurement was conducted at 750 K and 1.2 Torr by introducing $\sim 2 \times 10^{12}$ molecules cm^{-3} of 2(5H)-furanone (Sigma-Aldrich, purity >98%) to the flow reactor with helium bath gas being in excess. A relatively weak signal was observed for 2(5H)-furanone when a H_2-lamp (or an Ar-lamp) was

employed. However, in our kinetic measurements, the initial radical concentration is expected to be $[CH_2CHCHC(O)OCH_3]_{t=0} \approx 1–2 \times 10^{11}$ molecules cm^{-3}, and it could well be that our apparatus is not sensitive enough to observe 2-furanone (P1) at such low concentrations.

Experiments were also conducted to detect a possible product signal at $m/z = 68$ that, according to our calculations, corresponds to the mass of the reaction products of channels (2) and (3). However, as is shown in Figure 4, photolysis of the precursor at 248 nm already produces a signal at 612 K with sharp photolytic formation followed by a very slow formation. The very slow formation could originate from a product that is formed by a wall reaction of the studied radical. Remember that at 612 K the rate of thermal unimolecular decomposition is negligible. Interestingly, as temperature is increased to 750 K, the post-photolysis

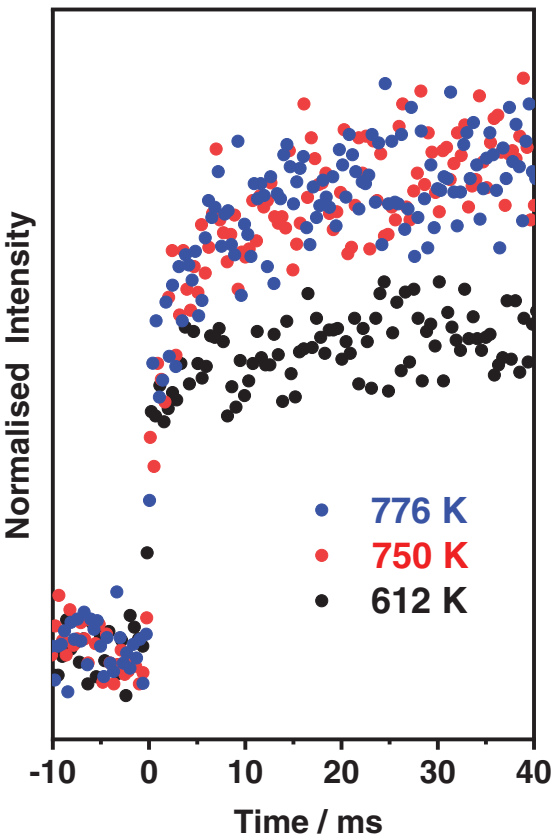

Fig. 4: A comparative plot for the signals observed at $m/z = 68$ at different temperatures ($p \approx 4$ Torr). Signal intensities before laser photolysis were used for signal normalization.

formation signal at $m/z = 68$ becomes more intense and faster. However, it is important to note that such an increase in the signal intensity cannot be used to draw any definite conclusions, since $m/z = 68$ may be produced also by other sources than reaction (1). Our PIMS apparatus is not able to detect methoxy radical (CH_3O, $m/z = 31$), which is the other product produced by channels (2) and (3), due to the combination of high ionization potential 10.7 eV [28] and low sensitivity of PIMS apparatus to detect CH_3O radical.

Our master equation model includes only the kinetically most favored channel (channel (1), see Figure 3). This was done because products of channels 2 and 3 ($P_2 + CH_3O$ and $P_3 + CH_3O$) were observed in preliminary MESMER simulations to exist too high in energy to explain the current experimental kinetic results. Employed L–J parameters associated with the collisions between modeled species (i.e. R, I_c) [15] and the bath gases (Helium and N_2) [24] are given in supplementary information (see Table S2).

The plots in Figure 5 show the measured thermal unimolecular decomposition rate coefficients of $CH_2CHCHC(O)OCH_3$ radical as function of helium and N_2 bath gas density, respectively. Also shown are the best fit results of MESMER simulations obtained by minimizing χ^2 using $TS1_c$ and $TS2_c$ barrier heights as well as the collisional energy transfer parameters $\Delta E_{\text{down, ref}}$ and n as variable parameters. MESMER simulation results are overall in good agreement with the measured rate coefficients. However, in order to obtain good agreement with the experimental results, the barrier heights of the $TS1_c$ and $TS2_c$ had to be reduced by 3.3 kcal/mol, while maintaining the energy gap between both the transition states. The reasoning behind lowering both barriers by the same amount is that the relative energies of stationary points along a PES computed using ab-initio quantum calculations are more reliable than their absolute energies. Without making such modification to the $TS1_c$ and $TS2_c$ barrier heights, the results of MESMER simulations would be on average ~80% lower than the experimental rate coefficients. The following (see also Table 2), optimized expressions were obtained for the energy transfer parameter

Tab. 2: The optimized collisional energy transfer parameter values for $\Delta E_{\text{down, ref}}$ and n as well as the corresponding χ^2/point, obtained by fitting against experimental results measured using helium and N_2 bath gases.

Bath gas	$\Delta E_{\text{down}} = \Delta E_{\text{down, ref}} \left(\frac{T}{T_{\text{ref}}}\right)^n$		
	$\Delta E_{\text{down, ref}}$	n	χ^2/point
Helium	152	0.33	24.2
N_2	211	0.12	12.6

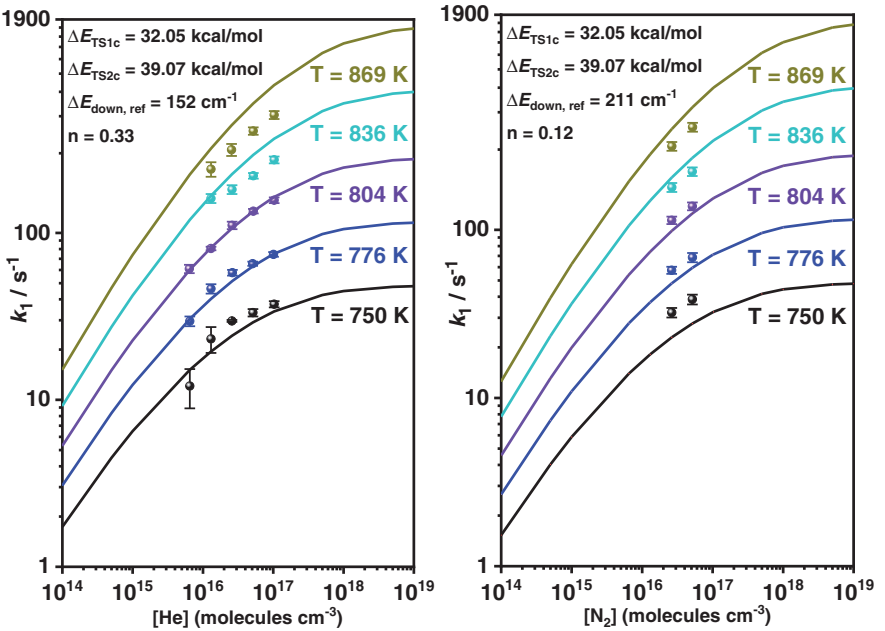

Fig. 5: Left- and right-hand side plots show the measured thermal unimolecular decomposition rate coefficients of $CH_2CHCHC(O)OCH_3$ radical as function of helium and N_2 bath gas density, respectively. Different temperature conditions are labeled as colored points. The results of MESMER simulations are shown as colored lines. The optimized collisional energy transfer parameters and the optimized $TS1_c$ and $TS2_c$ energies are shown on the top left corner of the plots.

ΔE_{down} depending upon the nature of bath gas (Helium or N_2): $(\Delta E_{\text{down}})_{\text{He}} = 152\left(\frac{T}{298}\right)^{0.33}$ cm^{-1} and $(\Delta E_{\text{down}})_{N_2} = 211\left(\frac{T}{298}\right)^{0.12}$ cm^{-1}.

The MESMER optimized $\Delta E_{\text{down, ref}}$ and n values for helium (152 cm^{-1} and 0.33) and N_2 (211 cm^{-1} and 0.12) bath gases are reasonable [24]. The results of our simulations are provided in ChemKin PLOG format in the supplementary material. The MESMER input file is also provided.

Figure 6 shows Arrhenius plots of reaction (1) measured in helium and nitrogen bath gases, where $k_1^{\circ} = k_1/[\text{bath gas}]$ are plotted as function of temperature. It is apparent from Figure 6 that the obtained k_1° values do not converge in employed bath gas density ranges 0.6–10 $\times$ 10^{16} molecules cm^{-3} (He) and 2.6–5 $\times$ 10^{16} molecules cm^{-3} (N_2). This shows that our measurements for reaction (1) are in the fall-off region, which is in agreement with the MESMER simulations shown in Figure 5.

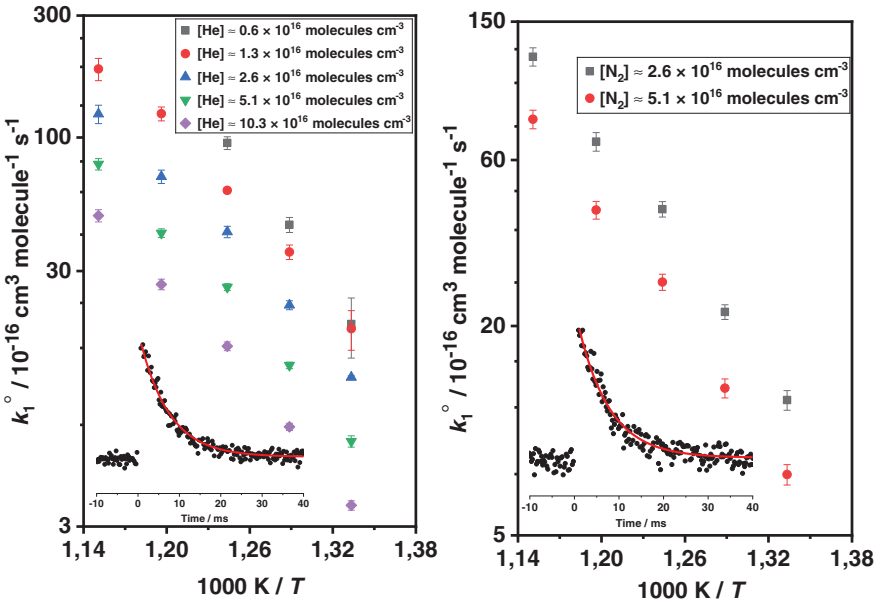

Fig. 6: On the left- and right-hand-side are the Arrhenius plots for the thermal unimolecular decomposition of $CH_2CHCHC(O)OCH_3$ radical measured in helium and N_2 bath gases, respectively. A typical $CH_2CHCHC(O)OCH_3$ radical decay profile and a corresponding single-exponential fit is shown in an inset of each plot.

5 Conclusion

We have measured the thermal unimolecular decomposition kinetics of $CH_2CHCHC(O)OCH_3$ radical as function of temperature (750–869 K) and bath gas density (0.6–10 $\times$ 10^{16} molecules cm^{-3}). Both helium and nitrogen bath gases were used. In addition, we determined a low upper limit value for the bimolecular rate coefficient of the $CH_2CHCHC(O)OCH_3$ + O_2 reaction at 600 K ($k_2 \leq 7.5 \times 10^{-17}$ cm^3 $molecule^{-1}$ s^{-1}). The measured unimolecular decomposition rate coefficients were in the range 10–500 s^{-1} in the experimental temperatures, suggesting that the decomposition reaction may be an important loss pathway for the resonantly-stabilized $CH_2CHCHC(O)OCH_3$ radical under LTC ($T < 1000$ K) and high temperature combustion conditions. No definite evidence of reaction products was obtained experimentally, potentially due to our apparatus being probably too insensitive to observe the plausible product (2-Furanone). The experiments were complemented with quantum chemical calculations and master equation simulations using the MESMER code. The master equation model was optimized by fitting the collisional energy transfer parameters $\Delta E_{down,\ ref}$ and n as

well as the $TS1_c$ and $TS2_c$ barrier heights (reduced by ~3 kcal/mol). The simulations returned reasonable values for the $\Delta E_{\text{down, ref}}$ parameter (152 and 211 cm^{-1} for helium and N_2 bath gases, respectively) and values obtained for the parameter n (0.33 and 0.12) reflects that for both (helium and N_2) bath gases ΔE_{down} has small positive temperature dependency. The optimized master equation model is in good agreement with the experimental results. The experimentally constrained master equation model was used to simulate thermal unimolecular decomposition kinetics of $CH_2CHCHC(O)OCH_3$ radical at pressures and temperatures relevant for autoignition, LTC, and high-temperature combustion. The simulation results are provided in the ChemKin compatible PLOG format.

6 Supporting information

Optimized geometries and associated energies of the stationary points on the PES of reaction (1), measured ion signal profiles at $m/z = 47$ and 141, k_1 vs. 1000 K/T figure to test (O_2) and (precursor) dependencies, L–J parameters of the bath gases and modeled species, MESMER input files (MESMER.xml), and PLOG files.

Acknowledgment: S.P.J. and A.J.E. acknowledge support from the Academy of Finland, Funder Id: http://dx.doi.org/10.13039/501100005877, Grant numbers 294042/319353 and 288377. P.S. acknowledges support from the BiofCFD project of the INNO INDIGO ERA-Net S&T Energy 2016 bio-based energy program funded by the Academy of Finland, grant number 311967. T.T.P. acknowledges support from the Funder Name: Helsingin Yliopisto, Funder Id: http://dx.doi.org/10.13039/100007797, Doctoral Programme in Chemistry and Molecular Sciences of the University of Helsinki. Computational resources were provided by CSC IT Centre for Science in Finland.

References

1. A. Demirbas, Energy Sources **29** (2007) 303.
2. A. Demirbas, Energy Policy **35** (2007) 4661.
3. S. T. Keera, S. M. El Sabagh, A. R. Taman, Fuel **90** (2011) 42.
4. A. K. Agarwal, Prog. Energy Combust. Sci. **33** (2007) 233.
5. C. K. Westbrook, Annu. Rev. Phys. Chem. **64** (2013) 201.
6. O. Herbinet, W. J. Pitz, C. K. Westbrook, Combust. Flame **154** (2008) 507.
7. C. J. Mueller, W. J. Cannella, J. T. Bays, T. J. Bruno, K. DeFabio, H. D. Dettman, R. M. Gieleciak, M. L. Huber, C. B. Kweon, S. S. McConnell, W. J. Pitz, M. A. Ratcliff, Energy Fuels **30** (2016) 1445.
8. S. Gaïl, S. Sarathy, M. Thomson, P. Diévart, P. Dagaut, Combust. Flame **155** (2008) 635.

9. S. Sarathy, S. Gaïl, S. Syed, M. Thomson, P. Dagaut, Proc. Combust. Inst. **31** (2007) 1015.
10. B. Yang, C. K. Westbrook, T. A. Cool, N. Hansen, K. Kohse-Höinghaus, Proc. Combust. Inst. **34** (2013) 443.
11. Y. L. Wang, Q. Feng, F. N. Egolfopoulos, T. T. Tsotsis, Combust. Flame **158** (2011) 1507.
12. V. B. Oyeyemi, J. A. Keith, E. A. Carter, J. Phys. Chem. A **118** (2014) 7392.
13. H. K. Ng, S. Gan, J.-H. Ng, K. M. Pang, Fuel **104** (2013) 620.
14. H. Bennadji, L. Coniglio, F. Billaud, R. Bounaceur, V. Warth, P. A. Glaude, F. Battin-Leclerc, Int. J. Chem. Kinet.**43** (2011) 204.
15. X. Zhou, Y. Zhai, L. Ye, L. Zhang, Sustain. Energy Fuels **2** (2018) 392.
16. V. D. Knyazev, I. R. Slagle, J. Phys. Chem. A **102** (1998) 8932.
17. A. Eskola, R. Timonen, Phys. Chem. Chem. Phys. **5** (2003) 2557.
18. V. D. Knyazev, Á. Bencsura, I. R. Slagle, J. Phys. Chem. A **101** (1997) 849.
19. J. L. Bao, J. Zheng, I. M. Alecu, B. J. Lynch, Y. Zhao, D. G. Truhlar, Database of Frequency Scale Factors for Electronic Model Chemistries (Version 3 Beta 2) (2017).
20. D. G. Liakos, F. Neese, J. Phys. Chem. A **116** (2012) 4801.
21. F. Neese, WIREs Comput. Mol. Sci. **2** (2012) 73.
22. M. J. Frisch, G. W. Trucks, H. B. Schlegel, G. E. Scuseria, M. A. Robb, J. R. Cheeseman, G. Scalmani, V. Barone, G. A. Petersson, H. Nakatsuji, X. Li, M. Caricato, A. V. Marenich, J. Bloino, B. G. Janesko, R. Gomperts, B. Mennucci, H. P. Hratchian, J. V. Ortiz, A. F. Izmaylov, J. L. Sonnenberg, Williams, F. Ding, F. Lipparini, F. Egidi, J. Goings, B. Peng, A. Petrone, T. Henderson, D. Ranasinghe, V. G. Zakrzewski, J. Gao, N. Rega, G. Zheng, W. Liang, M. Hada, M. Ehara, K. Toyota, R. Fukuda, J. Hasegawa, M. Ishida, T. Nakajima, Y. Honda, O. Kitao, H. Nakai, T. Vreven, K. Throssell, J. A. Montgomery Jr., J. E. Peralta, F. Ogliaro, M. J. Bearpark, J. J. Heyd, E. N. Brothers, K. N. Kudin, V. N. Staroverov, T. A. Keith, R. Kobayashi, J. Normand, K. Raghavachari, A. P. Rendell, J. C. Burant, S. S. Iyengar, J. Tomasi, M. Cossi, J. M. Millam, M. Klene, C. Adamo, R. Cammi, J. W. Ochterski, R. L. Martin, K. Morokuma, O. Farkas, J. B. Foresman, D. J. Fox, Gaussian 16 Rev. A.03, Wallingford, CT (2016).
23. R. Van de Vijver, J. Zádor, Comput. Phys. Commun. **248** (2020) 106947.
24. D. R. Glowacki, C.-H. Liang, C. Morley, M. J. Pilling, S. H. Robertson, J. Phys. Chem. A **116** (2012) 9545.
25. S. P. Joshi, T. T. Pekkanen, R. S. Timonen, A. J. Eskola, J. Phys. Chem. A **123** (2019) 10514.
26. V. D. Knyazev, I. R. Slagle, J. Phys. Chem. A **102** (1998) 1770.
27. K. Wang, S. M. Villano, A. M. Dean, Phys. Chem. Chem. Phys. **17** (2015) 6255.
28. S. G. Lias, In: NIST Chemistry WebBook, NIST Standard Reference Database Number 69, P. J. Linstrom, W. G. Mallard (Eds.). National Institute of Standards and Technology, Gaithersburg, MD (2005), P. 20899.

Supplementary Material: The online version of this article offers supplementary material (https://doi.org/10.1515/zpch-2020-1612).